

Detection of Single Atoms and Buried Defects in Three Dimensions by Aberration-Corrected Electron Microscope with 0.5-Å Information Limit

C. Kisielowski,¹ B. Freitag,⁵ M. Bischoff,⁵ H. van Lin,⁵ S. Lazar,⁵ G. Knippels,⁵ P. Tiemeijer,⁵ M. van der Stam,⁵ S. von Harrach,⁵ M. Stekelenburg,⁵ M. Haider,⁶ S. Uhlemann,⁶ H. Müller,⁶ P. Hartel,⁶ B. Kabius,² D. Miller,² I. Petrov,³ E.A. Olson,³ T. Donchev,³ E.A. Kenik,⁴ A.R. Lupini,⁴ J. Bentley,⁴ S.J. Pennycook,⁴ I.M. Anderson,⁴ A.M. Minor,¹ A.K. Schmid,¹ T. Duden,¹ V. Radmilovic,¹ Q.M. Ramasse,¹ M. Watanabe,¹ R. Erni,¹ E.A. Stach,¹ P. Denes,¹ and U. Dahmen^{1,*}

¹National Center for Electron Microscopy, Lawrence Berkeley National Laboratory, One Cyclotron Rd., Berkeley, CA 94720, USA

²Argonne National Laboratory, Electron Microscopy Center, Argonne, IL 10329, USA

³Center for Microanalysis of Materials, University of Illinois, 104 S. Goodwin Avenue, Urbana, IL 61801, USA

⁴Materials Science and Technology Division, Oak Ridge National Laboratory, P.O. Box 2008, Oak Ridge, TN 37831, USA

⁵FEI Company, Eindhoven, Building AAE, Achtseweg Noord 5, P.O. Box 80066, 5600 KA Eindhoven, The Netherlands

⁶CEOS GmbH, Englerstr. 28, D-69126 Heidelberg, Germany

Abstract: The ability of electron microscopes to analyze all the atoms in individual nanostructures is limited by lens aberrations. However, recent advances in aberration-correcting electron optics have led to greatly enhanced instrument performance and new techniques of electron microscopy. The development of an ultrastable electron microscope with aberration-correcting optics and a monochromated high-brightness source has significantly improved instrument resolution and contrast. In the present work, we report information transfer beyond 50 pm and show images of single gold atoms with a signal-to-noise ratio as large as 10. The instrument's new capabilities were exploited to detect a buried $\Sigma 3$ {112} grain boundary and observe the dynamic arrangements of single atoms and atom pairs with sub-angstrom resolution. These results mark an important step toward meeting the challenge of determining the three-dimensional atomic-scale structure of nanomaterials.

Key words: aberration-correcting optics, sub-angstrom, TEM/STEM, atomic structure, buried defect

INTRODUCTION

The atom-by-atom analysis of individual nanostructures is an important goal in nanoscience that was first formulated by Richard Feynman in his famous 1959 lecture, “There’s Plenty of Room at the Bottom” (Feynman, 1960). Feynman proposed that one could analyze any substance simply by looking to see where the atoms are: “I put this out as a challenge: Is there no way to make the electron microscope more powerful?” Despite major progress, Feynman’s challenge to electron microscopy is still out of reach. The fundamental barrier to improving the electron microscope has been the presence of unavoidable aberrations in rotationally symmetric electromagnetic lenses (Scherzer, 1936). The Transmission Electron Aberration-corrected Micro-

scope (TEAM) project is a collaborative effort to redesign the electron microscope around aberration-corrected optics (<http://ncem.lbl.gov/TEAM-project/>) in order to extend the spatial resolution to 50 pm, improve contrast, stability, sensitivity, brightness, and energy resolution.

Using a prototype instrument constructed under this project, we have demonstrated information transfer to below 50 pm in both the scanning probe (scanning transmission electron microscope (STEM)) and fixed-beam (transmission electron microscope (TEM)) modes of transmission electron microscopy. The detection of GaN (555) and Au (660) image Fourier components in STEM images at 49 and 48 pm, respectively, and the extension of Young fringes to below 50 pm in TEM mode represent major improvements.

A 50-pm information limit implies a focal spread of the electron beam of only about 1 nm in parallel-beam operation, resulting in greatly improved signal-to-noise (S/N) ratio and depth precision. In this article, we describe examples that take advantage of the instrument’s performance to

Received July 9, 2008; accepted July 23, 2008

*Corresponding Author. E-mail: UDahmen@lbl.gov

image a buried interface and to observe the motion of individual atoms with great sensitivity to their position along the beam direction.

MICROSCOPE, MATERIALS, AND METHODS

The TEAM 0.5 microscope is based on a commercially available FEI Titan 80-300 (scanning) TEM platform. The microscope is located in a separate room within a sound-proof enclosure and operated remotely. Standard instrument alignments are performed with the aid of a high-sensitivity camera that transfers the information on the fluorescent screen in real time to the graphical user interface. The electron source of TEAM 0.5 consists of a novel high-brightness Schottky-type field emission gun and a Wien-filter type monochromator (Tiemeijer, 1999). At an energy spread of 0.8 eV (full width at half maximum (FWHM)), the brightness of the gun exceeds 4.5×10^9 A/cm²/srad at 300 kV. The electron monochromator can reduce the energy spread to 0.13 and 0.08 eV at 300 and 80 kV, respectively. The condenser lens system is the standard three-condenser lens system of the Titan 80-300 column that provides variable probe-convergence angles in STEM mode and adjustable parallel illumination in TEM mode. A novel aberration corrector from CEOS GmbH corrects for objective-lens illumination aberrations (Haider et al., 2000; Müller et al., 2006). The objective lens is a high-resolution twin-type lens (UltraTwin) with an inherent third-order spherical aberration coefficient $C_3 (= C_s)$ of 0.66 mm (300 kV), and a (relativistic) coefficient of chromatic aberration C_c of 1.64 mm. The imaging aberration corrector is a hexapole-type corrector from CEOS GmbH (Haider et al., 1998). The system includes a retractable Gatan US1000 slow-scan charge-coupled device (CCD) camera and a high-resolution GIF Tridiem 866. In its current configuration, TEAM 0.5 is operated either at 300 or 80 kV. All optical elements are activated, independent of the operation mode, including both aberration correctors. Thus, switching between different operation modes at a selected microscope high tension does not change the thermal load on the system.

Both aberration correctors on TEAM 0.5, i.e., for illumination and for imaging, correct for coherent lens aberrations, in particular the spherical aberration of the objective lens, and partially for higher-order aberrations and resulting parasitic aberrations. Although coherent aberrations are corrected to a large extent, the corrector units increase slightly the chromatic aberration of the system. The inherent C_c of the objective lens of 1.64 mm increases to ~ 2.1 mm with the correctors activated, both for TEM and STEM operating modes.

The illumination aberration corrector is an improved version of the hexapole corrector (Haider et al., 2000)

Table 1. Typical Residual Axial Aberration Coefficients (without Azimuth Angle) of the Illumination Aberration Corrector and the Imaging Aberration Corrector of TEAM 0.5 for Operation at 300 kV.*

Aberration coefficient	Illumination (nm)	Imaging (nm)
Defocus C1	NA ^a	NA ^a
Twofold astigmatism A1	NA ^a	NA ^a
Threefold astigmatism A2	24	43
2nd-order coma B2	8	38
3rd-order spherical aberration C3	−150	−341
Fourfold astigmatism A3	97	1.0e3
3rd-order star aberration S3	90	921
Fivefold astigmatism A4	10.2e3	13.4e3
4th-order three-lobe aberration D4	7.2e3	3.3e3
4th-order coma B4	5.5e3	8.0e3
5th-order spherical aberration C5	508e3	5.1e6
Sixfold astigmatism A5	220e3	1.4e6
5th-order rosette aberration R5	24e6	153e3
5th-order star aberration S5	6.6e6	430e3

*First-order aberrations, C1 and A1, are manually optimized.

^aNA = not applicable.

suitably upgraded to minimize the impact of sixfold astigmatism A5 (Müller et al., 2006). It is configured to fully correct the set of coherent axial aberrations up to 4th order including 5th-order spherical aberration C5 and sixfold astigmatism A5. Table 1 provides a list of typical residual aberration coefficients that are measured after fine-tuning of the corrector at 300 kV. The aberration phase shifts due to this set of residual aberrations are illustrated in Figure 1a. Although a phase shift of $\pi/4$ is reached at an illumination semiangle of 25.2 mrad, the calculated phase plate in Figure 1a reveals that to minimize the effect of the diffraction limit on resolution, no substantial impact due to residual aberrations is anticipated if the illumination angle is increased to ~ 30 mrad.

The imaging aberration corrector fully corrects for coherent axial aberrations up to 3rd order and partially compensates for 4th- and 5th-order aberrations. Whereas off-axial aberrations are negligible for the illumination aberration corrector, they must be considered in the setup of the imaging corrector. To minimize the impact of isotropic off-axial coma B3c, and hence to maximize the number of equally resolved image points, the imaging corrector is adjusted such that the 5th-order spherical aberration is finite positive (see Table 1). Figure 1b illustrates the phase shifts due to the residual axial aberrations given in Table 1, revealing that a $\pi/4$ phase shift is reached at 15.9 mrad. The “aberration-free” area in the imaging mode is thus smaller than in the illumination mode (25.2 mrad). This is due to the fact that it is possible to compensate 4th-order aberrations, sixfold astigmatism A5, and 5th-order spherical aber-

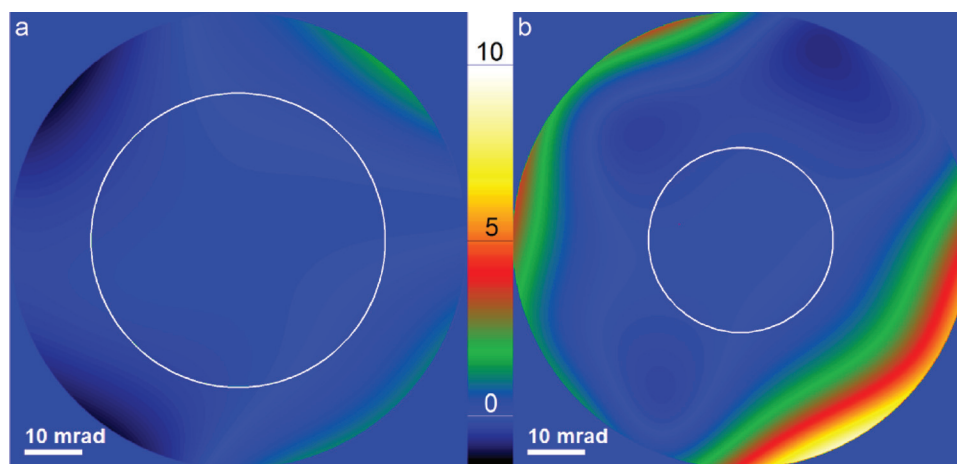


Figure 1. Phase shifts due to residual coherent aberrations of TEAM 0.5: (a) illumination mode and (b) imaging mode. The color scale bar gives the phase shifts in units of π . The angular areas displayed have a radius of 39.3 mrad. The white circles mark the angle where a phase shift of $\pi/4$ is reached. For the illumination, this occurs at 25.2 mrad, whereas for the imaging this occurs at 15.9 mrad.

ration C5 with the improved illumination aberration corrector, but these coefficients, including 3rd-order aberrations, are larger on the imaging side.

In STEM mode, we employ the illumination aberration corrector to reduce the effect of coherent aberrations on the electron probe and to increase the probe convergence angle such that both lateral and depth resolution are improved (van Benthem et al., 2006). The electron probe that provided the highest lateral resolution was obtained by using a semiconvergence angle of 30 mrad, which enabled a probe current of ~ 50 pA. For this setting, even without employing the monochromator, the chromatic aberration due to an inherent energy spread of ~ 0.8 eV (FWHM) does not severely affect the probe size. Figure 2 shows a high-angle annular-dark-field (HAADF) STEM image of wurtzite GaN. In this [211] projection, the distance between two nearest Ga atoms is 63 pm (see inset). As seen in the line profile extracted from this image, the 63-pm dumbbell spacing is clearly resolved (Fig. 2c). Note that the N columns are not directly resolved in these images due to their much lower atomic number. However, the line traces show an asymmetry in the shoulder below the peaks that is due to the presence of N. This effect becomes more noticeable at higher S/N levels when images are statistically averaged. In addition, information transfer to below 50 pm is visible in the Fourier transform of this and other STEM images (Fig. 2b,d). Line traces from two such transforms demonstrate peaks at 49 pm (GaN) and 48 pm (Au) (Fig. 2d). (For a discussion of the relationship between information transfer and resolution, see den Dekker & van den Bos, 1997; Van Aert et al., 2006; Peng et al., 2008.)

In the TEM mode, we employ the imaging aberration corrector in combination with the monochromator to reduce the effect of chromatic aberrations on aberration-

corrected imaging. The monochromator was set up to obtain an energy spread ΔE at the sample of less than 0.2 eV. Figure 3 shows calculated TEM phase contrast transfer functions for the residual aberrations given in Table 1 for a nonmonochromated beam and for a monochromated beam. According to Figure 3, the experimentally measured energy spread should enable an information limit of better than 50 pm, i.e., the information transfer is not impacted by the chromatic aberration, but solely by potential residual instabilities.

The extent of information transfer is often measured in frequency space using Young's fringes produced by an image shift during exposure. Figure 4 shows the Fourier transforms of high-resolution TEM images of a gold test sample supported on an amorphous carbon film. Without the monochromator, the Young's fringes extend only to just beyond 70 pm (Fig. 4a). Upon reducing the effect of chromatic aberration by the use of the monochromator, the Young's fringes are seen to extend beyond the 50-pm limit (red circle) in all directions, demonstrating that this microscope is capable of 50-pm resolution. The experiment indicates that further improvements can be expected from C_c correction and more accurate control of higher order aberrations, which will be incorporated at a later stage in the project.

For comparison with experiments, multislice image simulations were performed (Cowley & Moodie, 1957), using the MacTempas image simulation program (<http://www.totalresolution.com/>). Typical TEM simulation parameters included a spherical aberration C_s of 0.003 mm, a beam divergence of 0.15 mrad, a focus spread of 0.8 nm, a lens aperture radius of 20 nm^{-1} , and a Debye-Waller factor of 0.02 nm^2 . No absorption was included. These simulations indicated that the dominant aberrations that affected

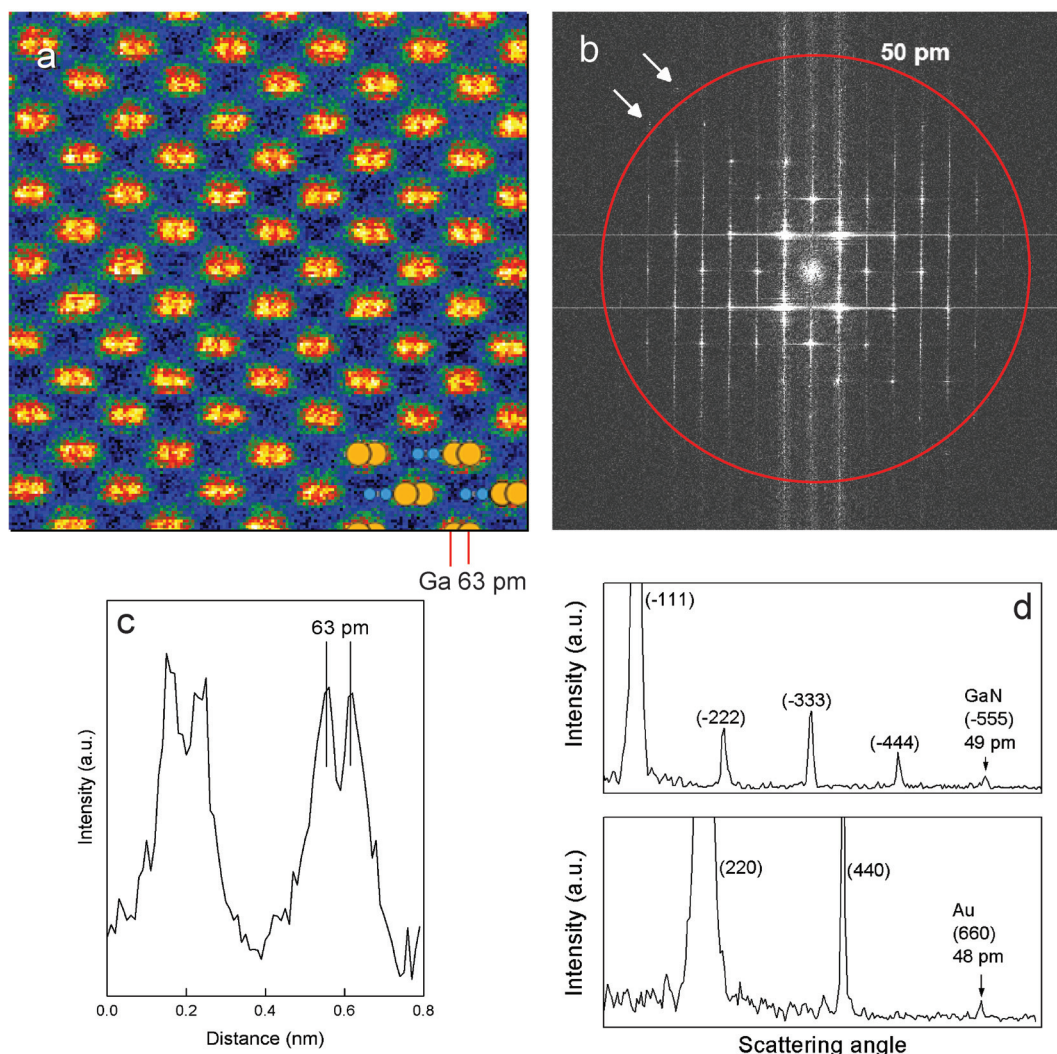


Figure 2. STEM performance. **a:** HAADF STEM image of wurtzite GaN [211]; crystal structure shown in the inset indicates Ga dumbbell spacing of 63 pm in this projection. **b:** Fourier transform of the image; image Fourier components extend to below 50 pm. **c:** Line trace across GaN dumbbells revealing 63-pm atom column separations. **d:** Single pixel line profiles from image Fourier transforms, shown here for Au [111] and GaN [211], demonstrating image Fourier components below 50 pm with S/N ratios around 3.

image intensities could be modeled approximately by a residual twofold astigmatism of 3.5 ± 0.8 nm ($102 \pm 8^\circ$) and a 5th-order spherical aberration coefficient set to 20 mm. In this work we account for the presence of residual twofold astigmatism by a focus error of ~ 1 nm with respect to theory. An attenuation factor in the form of mechanical vibrations of 35 pm (peak to peak) was used to eliminate high-frequency Fourier components from the simulations. This factor coincides with the limit for nonlinear information transfer (Bals et al., 2005) in this microscope, which, in the best cases, allowed recording of Au (880) image Fourier components at 36 pm. Residual aberrations, vibrations, and other factors such as the modulation transfer function of the CCD camera can also affect this attenuation. Image focus values were determined by reconstruction of the

electron exit-surface wave function (Coene et al., 1992) from a focus series of images. In this process, we control the focus stability in successively recorded images to about 0.2 nm. Reconstruction was followed by exit-wave propagation to extract local focus values close to the areas of interest by maximizing phases in focal steps of 0.1 nm.

RESULTS AND DISCUSSION

The demonstrated information transfer represents a major advance beyond the state of the art (Smith, 1997; Kisielowski et al., 2001; Kimoto et al., 2007; Sawada et al., 2007; Hetherington et al., 2008; Lentzen, 2008; Muller et al., 2008; Nellist

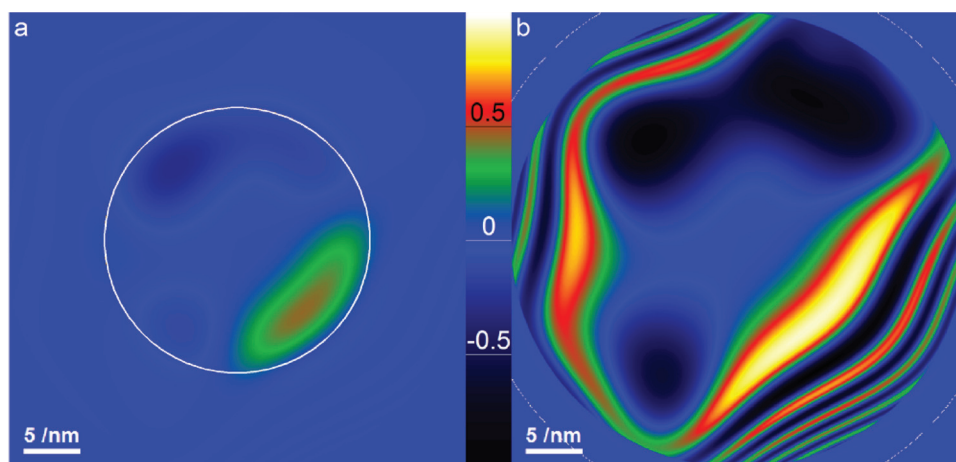


Figure 3. TEM transfer functions. The angular areas displayed have a radius of 39.3 mrad, corresponding to 50 pm at 300 kV. **a:** Shows the transfer function at 300 kV for the aberration coefficients given in Table 1 and for an energy spread ΔE of 0.8 eV. The transfer is limited by damping due to ΔE and chromatic aberration ($C_c = 2.1$ mm), resulting in a theoretical information limit of 86 pm (white circle). **b:** Shows the same transfer function for a monochromated beam with 0.2-eV energy spread. The (optical) information limit is at 43 pm, i.e., beyond the 50-pm area displayed.

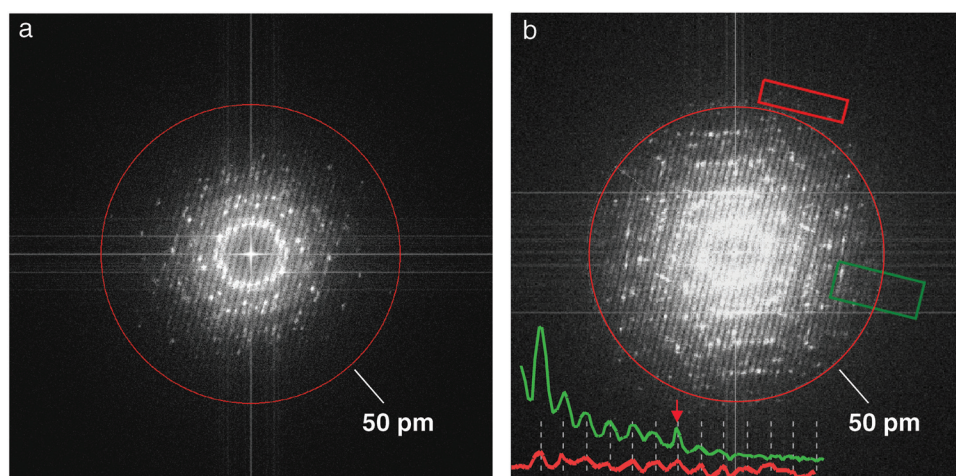


Figure 4. TEM performance using Young's fringe experiments with gold nanoparticles suspended on a carbon film: **(a)** with monochromator switched off, the fringes extend to about 70 pm; **(b)** with monochromator switched on; inset line traces are taken from the areas outlined in green and red boxes and show that the fringes extend beyond 50 pm. In the line traces, the periodicity of the Young's fringes is marked with dashed lines. The arrow indicates where the green trace crosses the 50-pm circle.

et al., 2004; Smith, 2008). This capability enables new types of experiments that require previously unavailable information transfer, precision, and signal-to-noise to explore depth information from two-dimensional images.

In the STEM mode, depth sectioning can be achieved using a focal series (Borisevich et al., 2006) or confocal electron microscopy (Frigo et al., 2002; Nellist et al., 2008). By exploiting the small focal depth of the microscope, it becomes possible to retrieve detailed structural information

from within the crystal volume. Figure 5 shows HAADF STEM images of a gold [111] crystal with the electron beam focused on the crystal surface (Fig. 5a) and defocused by 6 nm (Fig. 5b). An extended crystal defect—a buried $\Sigma 3$ {112} grain boundary—is visible only if the beam is focused into the crystal. At this specific defocus, the presence of a microfaceted boundary with alternating {112} segments joined at sharp edges becomes clearly apparent (Westmacott et al., 1999). From calculated probe profiles, we estimate a

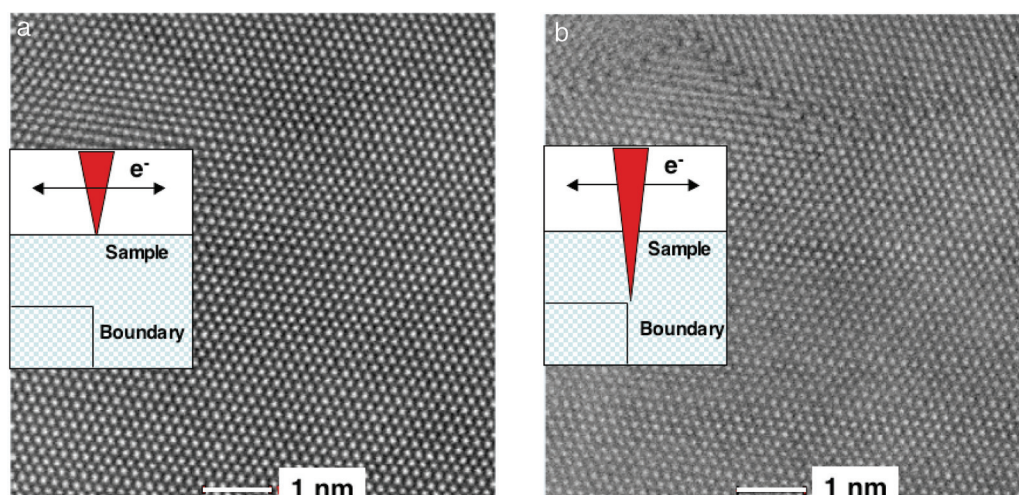


Figure 5. HAADF STEM images of gold [111]: (a) STEM probe focused on sample surface as indicated by the schematic; (b) $\Sigma 3$ {112} grain boundary in the lower section of the foil (see inset schematic) is revealed only when the probe is focused 6 nm into the sample.

possible depth precision significantly better than 6 nm that is ultimately limited by noise.

The sensitivity achievable in TEM mode is explored further by analyzing the four lattice images of a nanobridge connecting two gold crystals, as shown in Figure 6. The images are part of a 15-member focal series recorded in the TEM mode (1-s exposures) at time intervals $\Delta t = 1.5$ s. Thus, the four images in Figure 6 show the structural evolution of the crystals recorded over 4.5 s at different focus values. Closer inspection of the images reveals a wealth of structural changes at the nanobridge/vacuum interfaces that were triggered by electron-beam excitation. The black arrows highlight the release of a single atom from a 2-atom column (Fig. 6a,b) leaving a single atom behind (Fig. 6c,d). The red arrows mark a row of thirteen 2-atom columns attached to a (111) crystal plane that bounds one side of the nanobridge. In a sudden burst, six columns disappear during observation (compare Fig. 6c,d images).

The line profiles from one of these images, shown in Figure 7a, demonstrate that a single gold atom is recorded with a S/N ratio of 10 and attenuates the incoming electron beam by $\sim 25\%$. Two-atom columns almost double this attenuation—this feature of the gold [110] system allows us to identify single gold atoms independent of any scaling factor in multislice calculations. The signal-to-noise ratio was measured in the vacuum region of Figure 6, with a mean intensity I_{mean} (typically 2600 counts) and a standard deviation (typically 70 counts). The contrast of atomic columns was then characterized by $1 - I_{\text{center}}/I_{\text{mean}}$, where I_{center} is the intensity minimum in the center of a column measured on a single pixel. Thus, our S/N values are based on single pixel measurements and can be improved by considering, for example, the fitting of a model function to a larger number of pixels around an intensity minimum.

To compare the measured contrast with simulations, the defocus was determined for the entire 15-member focal series by minimizing the deviation of calculated lattice images from a reconstructed exit-surface wave function and the experimental lattice images utilizing a Gerchberg-Saxton algorithm (Hsieh et al., 2004). As shown in Figure 7b, image focus values are stable to within ± 0.2 nm. Using the experimentally determined errors in contrast and defocus, we can make quantitative comparisons with extensive image simulations as described in the Methods section. Figure 7c shows the calculated image contrast for one atom (lower band) or two atoms (upper band) as a function of defocus or Z-height. In this graph, the experimentally measured contrast from a specific atomic column (black arrow in the four members of the focal series shown in Fig. 6) is shown as four data points (labeled a–c). While the first two data points (a,b) lie in the 2-atom band, the last two data points (c,d) have clearly moved to the 1-atom band. This shows that the loss of one atom between images b and c in the focal series is measurable (see arrow), demonstrating single-atom sensitivity.

Figure 7c further illustrates that in the appropriate range the contrast can be highly sensitive to atomic position in the Z-direction (see the effect of a 0.6-nm change in Z-height indicated by red lines in the 2-atom band). This suggests the potential for using measured image contrast to understand changes in the number or position of atoms in an individual atomic column from single plan-view images, a capability that can be exploited to measure the three-dimensional (3D) dynamic behavior of atoms or atomic columns (Kisielowski, C., Specht, P., Freitag, B., & Erni, R., forthcoming).

The opposite side of the nanobridge displays thirteen 2-atom columns attached to a narrow (111) crystal facet that is only about 1 nm tall (see red arrows). Figure 6d

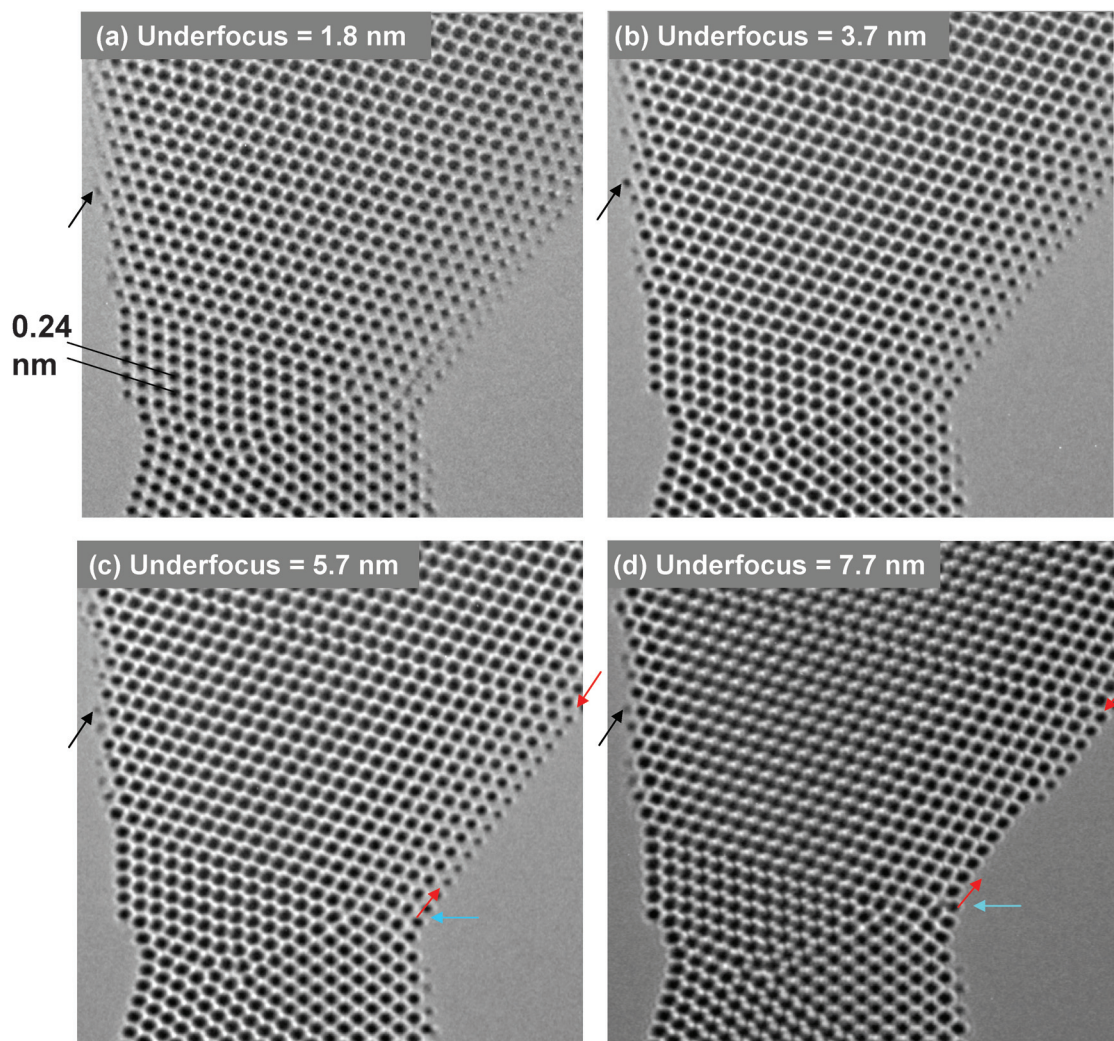


Figure 6. Four sequentially recorded TEM lattice images of gold [110] nanobridge connecting two grains that are rotated relative to each other by 90° around [110] axis. The four images shown are part of a 15-member focal series, recorded in time intervals of 1.5 s. Black arrows: (a,b) 2-atom column and (c,d) single atom. Red arrows: thirteen 2-atom columns, some of which disappear in d. Turquoise arrows: Rearrangement of atom columns at the intersection of a dissociated grain boundary with the surface. The focus difference on both sides of the bridge is negligible because the film was grown onto a flat single crystal substrate.

shows that six columns have disappeared under the influence of the electron beam. The origin of this process can be correlated with contrast details related to their relative Z-position, explored in detail elsewhere.

Other interesting physical processes are observable in these images, such as the rearrangement of atomic columns at the intersection of a dissociated grain boundary with the crystal surface (turquoise arrows), as well as the propagation of atomic steps on facets (not shown). Although these features are not addressed here, it is clear that the improved capabilities of the new microscope will enable direct atomic-level observation of phenomena such as crystal growth in three dimensions.

CONCLUSIONS

We have reported the successful construction and initial operation of an aberration-corrected STEM/TEM electron microscope with the potential for investigating crystal structures with a lateral resolution of 50 pm. In STEM mode, we have exploited its capability to resolve a lateral Ga atomic column spacing of 63 pm and to detect the presence of a buried $\Sigma 3$ {112} grain boundary in a plan-view configuration. In TEM mode, we utilized the instrument's extraordinary S/N ratio to identify single gold atoms and to study the time evolution of atom configurations at a nanobridge/

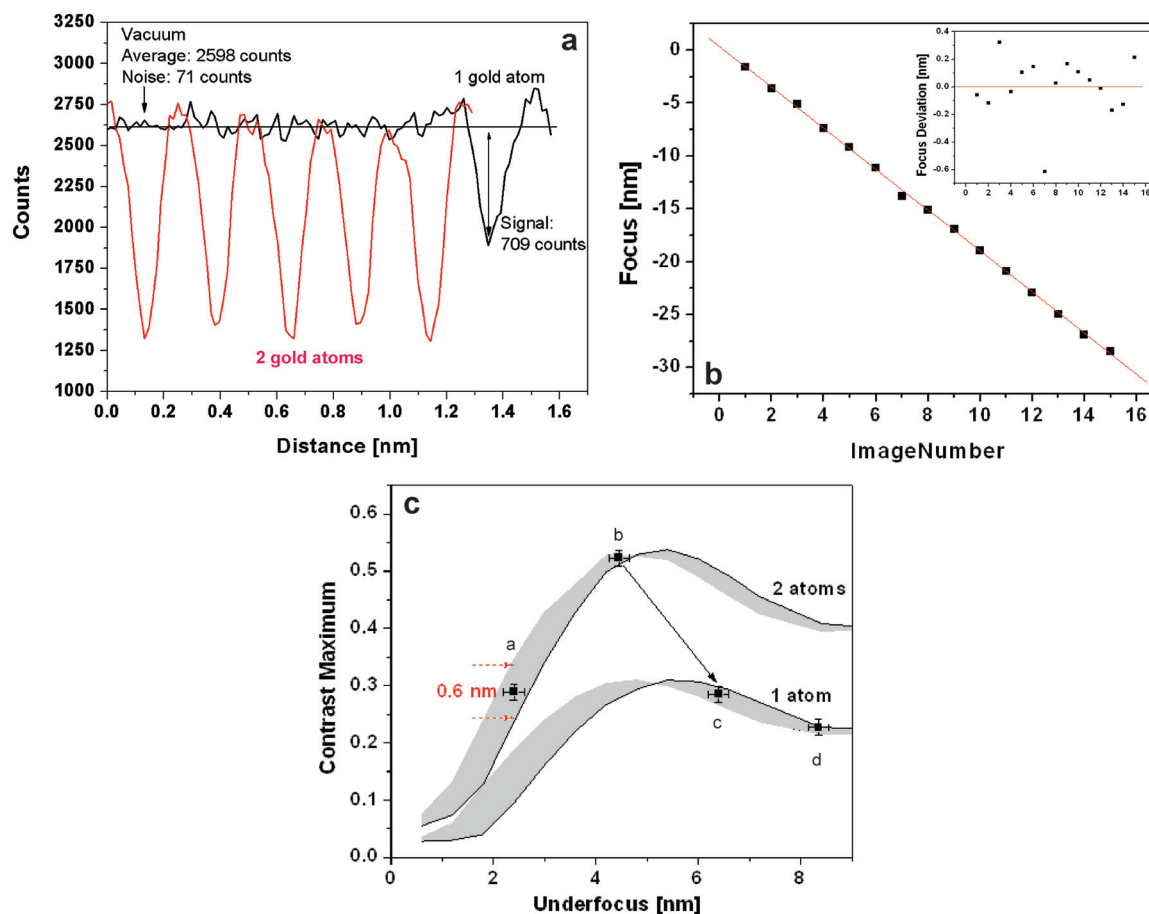


Figure 7. Quantitative data analysis. **a:** Line profiles with 45-pm integration width across the 2-atom columns (red), and single atom (black), marked with red and black arrows in Figure 6. The plot demonstrates S/N ratio of 10 for single gold atom at noise level of only 3%. **b:** Focus values for the 15-member through-focal series of lattice images of the nanobridge. The inset graph depicts a focus deviation of approximately ± 0.2 nm from a linear regression to the data. **c:** Contrast dependence on image focus/Z-position. Gray bands show calculated contrast dependence on Z-position of columns containing 1 and 2 gold atoms. Data points indicate the measured contrast of the column marked by a black arrow in Figure 6. The first two data points indicate a 2-atom column, while the last two data points correspond to single-atom contrast, confirming that a single gold atom has been lost between two exposures (Fig. 2b,c). The corresponding jump in intensity is marked with an arrow in the graph. To highlight the sensitivity to relative Z-position in this part of the curve, the calculated contrast variation of a 2-atom column for a Z-position change of 0.6 nm at a local underfocus of 2.4 nm is indicated by red lines.

vacuum interface. The new capabilities demonstrated in this report open a path toward atomic-resolution 3D tomography, which is one of the greatest challenges for electron microscopy and a key subject for future research in nanoscience and nanotechnology.

ACKNOWLEDGMENTS

The TEAM project is supported by the Department of Energy, Office of Science, Basic Energy Sciences.

REFERENCES

- BALS, S., KILAAS, R. & KISIELOWSKI, C. (2005). Nonlinear imaging using annular dark field TEM. *Ultramicroscopy* **104**, 281–289.
- BORISEVICH, A.Y., LUPINI, A.R., TRAVAGLINI, S. & PENNYCOOK, S.J. (2006). Depth sectioning of aligned crystals with the aberration-corrected scanning transmission electron microscope. *J Electron Microsc* **55**, 7–12.
- COENE, W., JANSSEN, G., OP DE BEECK, M. & VAN DYCK, D. (1992). Phase retrieval through focus variation for ultra-resolution in field-emission transmission electron microscopy. *Phys Rev Lett* **69**, 3743–3746.

- COWLEY, J.M. & MOODIE, A.F. (1957). The scattering of electrons by atoms and crystals. I. A new theoretical approach. *Acta Cryst* **10**, 609–619.
- DEN DEKKER, A.J. & VAN DEN BOS, A. (1997). Resolution: A survey. *J Opt Soc Am A* **14**, 547–557.
- FEYNMAN, R.P. (1960). There's plenty of room at the bottom. *Eng Sci* **23**, 22–23.
- FRIGO, S.P., LEVINE, Z.H. & ZALUZEC, N.J. (2002). Submicron imaging of buried integrated circuit structures using scanning confocal electron microscopy. *Appl Phys Lett* **81**, 2112–2114.
- HAIDER, M., UHLEMANN, S., SCHWAN, E., ROSE, H., KABUS, B. & URBAN, K. (1998). Electron microscopy image enhanced. *Nature* **392**, 768–769.
- HAIDER, M., UHLEMANN, S. & ZACH, J. (2000). Upper limits for the residual aberrations of a high-resolution aberration-corrected STEM. *Ultramicroscopy* **81**, 163–175.
- HETHERINGTON, C.J.D., CHANG, L.-Y., NELLIST, P.D., GONTARD, L.C., DUNIN-BORKOWSKI, R. & KIRKLAND, A.I. (2008). High-resolution TEM and the application of direct and indirect aberration-correction. *Microsc Microanal* **14**, 60–67.
- HSIEH, W.K., CHEN, F.R., KAI, J.J. & KIRKLAND, A.I. (2004). Resolution extension and exit wave reconstruction in complex HREM. *Ultramicroscopy* **98**, 99–114.
- KIMOTO, K., NAKAMURA, K., AIZAWA, S., ISAKOZAWA, S. & MATSUI, Y. (2007). Development of dedicated STEM with high stability. *J Electron Microsc* **56**, 17–20.
- KISIELOWSKI, C., HETHERINGTON, C.J.D., WANG, Y.C., KILAAS, R., O'KEEFE, M.A. & THUST, A. (2001). Imaging columns of the light elements carbon, nitrogen and oxygen with sub-Ångstrom resolution. *Ultramicroscopy* **89**, 243–263.
- LENTZEN, M. (2008). Contrast transfer and limits for sub-Ångstrom high-resolution transmission electron microscopy. *Microsc Microanal* **14**, 16–26.
- MULLER, A.D., FITTING KOURKOUTIS, L., MURFITT, M., SONG, J.H., HWANG, H.Y., SILCOX, J., DELLBY, N. & KRIVANEK, O.L. (2008). Atomic-scale chemical imaging of composition and bonding by aberration-corrected microscopy. *Science* **319**, 1073–1076.
- MÜLLER, H., UHLEMANN, S., HARTEL, P. & HAIDER, M. (2006). Advancing the hexapole C_s -corrector for the scanning transmission electron microscope. *Microsc Microanal* **12**, 442–455.
- NELLIST, P.D., CHISHOLM, M.F., DELLBY, N., KRIVANEK, O.L., MURFITT, M.F., SZILAGYI, Z.S., LUPINI, A.R., BORISEVICH, A., SIDES, W.H. & PENNYCOOK, S.J. (2004). Direct sub-ångstrom imaging of a crystal lattice. *Science* **305**, 1741.
- NELLIST, P.D., COSGRIFF, E.C., BEHAN, G. & KIRKLAND, A.I. (2008). Imaging modes for scanning confocal electron microscopy in a double aberration-corrected transmission electron microscope. *Microsc Microanal* **14**, 82–88.
- PENG, Y., OXLEY, M.P., LUPINI, A.R., CHISHOLM, M.F. & PENNYCOOK, S.J. (2008). Spatial resolution and information transfer in scanning transmission electron microscopy. *Microsc Microanal* **14**, 36–47.
- SAWADA, H., HOSOKAWA, F., KANEYAMA, T., ISHIZAWA, T., TERAOKA, M., KAWAZOE, M., SANNOMIYA, T., TOMITA, T., KONDO, Y., TANAKA, T., OSHIMA, Y., TANISHIRO, Y., YAMAMOTO, N. & TAKAYANAGI, K. (2007). Achieving 63pm resolution in scanning transmission electron microscope with spherical aberration corrector. *Japan J Appl Phys* **46**, L568–L570.
- SCHERZER, O. (1936). Über einige Fehler von Elektronenlinsen. *Z Phys* **101**, 593–603.
- SMITH, D.J. (1997). The realization of atomic resolution with the electron microscope. *Rep Prog Phys* **60**, 1513–1580.
- SMITH, D.J. (2008). Development of aberration-corrected electron microscopy. *Microsc Microanal* **14**, 2–15.
- TIEMEIJER, P.C. (1999). Measurement of Coulomb interactions in an electron beam monochromator. *Ultramicroscopy* **78**, 53–62.
- VAN AERT, S., VAN DYCK, D. & DEN DEKKER, A.J. (2006). Resolution of coherent and incoherent imaging systems reconsidered—Classical criteria and a statistical alternative. *Optics Expr* **14**, 3830–3839.
- VAN BENTHEM, K., LUPINI, A.R., OXLEY, M.P., FINDLAY, S.D., ALLEN, L.J. & PENNYCOOK, S.J. (2006). Three-dimensional ADF imaging of individual atoms by through-focal series scanning transmission electron microscopy. *Ultramicroscopy* **106**, 1092.
- WESTMACOTT, K.H., HINDERBERGER, S., RADETIC, S.T. & DAHMEN, U. (1999). PVD growth of fcc metal films on single crystal Si and Ge substrates. *Mat Res Soc Symp Proc* **562**, 93–102.